Materials Science & Engineering A 684 (2017) 394–405

Contents lists available at ScienceDirect

Materials Science & Engineering A

journal homepage: www.elsevier.com/locate/msea

Coarsening process and precipitation hardening in Fe_2AlV-strengthened ferritic $Fe_{76}Al_{12}V_{12}$ alloy

P.A. Ferreirós[a,b], P.R. Alonso[a], G.H. Rubiolo[a,c,*]

[a] Gerencia Materiales (GAEN) - Comisión Nacional de Energía Atómica (CNEA), Instituto Sabato - Universidad Nacional de San Martín (UNSAM), Av. Gral. Paz 1499, San Martín, Buenos Aires B1650KNA, Argentina

[b] Universidad Tecnológica Nacional, Facultad Regional General Pacheco (UTN-FRGP), Av. Hipólito Yrigoyen 288, Gral. Pacheco, B1617FRP Buenos Aires, Argentina

[c] Consejo Nacional de Investigaciones Científicas y Técnicas (CONICET), Godoy Cruz 2290, C1425FQB Ciudad Autónoma de Buenos Aires, Argentina

ARTICLE INFO

Keywords:
Ferrous alloy
Age hardening
Coarsening
Electron microscopy
Hardness measurement

ABSTRACT

Strengthening through a homogeneous distribution of a nano-sized second phase is a concept that is proposed to reinforce solid-solution body centered-cubic iron for high-temperature application in fossil-energy power plants. It was shown that these microstructures can be obtained in the Fe-Al-V system with $L2_1$-ordered Fe_2AlV precipitates in a ferritic matrix. The effect of aging in the range 600–700 °C on the ferritic $Fe_{76}Al_{12}V_{12}$ alloy was investigated using Vickers micro-hardness test and transmission electron microscopy. The diffusion screening coarsening theory is used to analyze the ripening kinetics. When volume fraction and mobility of the components in the ternary alloy are considered, the interfacial energy between the matrix and the precipitate was determined as $(18 \pm 3)\times10^{-3} J/m^2$ at 700 °C but increases strongly when the temperature decreases. A classic precipitation hardening behavior has been observed along the time for each aging treatment. At room temperature, the increment of flow stress has a peak of about 450 MPa for a precipitate radius of 10 nm. Quantitative agreement is found with strength values predicted from order strengthening theory, predicting that strength is controlled by a precipitate shearing mechanism for sizes around that of peak strengthening, and the Orowan dislocation bypass mechanism for larger sizes. The APB energy of Fe_2AlV precipitate was estimated to be $(27 \pm 4)\times10^{-2} J/m^2$.

1. Introduction

Ferritic steels are an attractive alternative to austenitic steels for high-temperature applications (e.g., in thermal power plants) due to their lower cost and thermal expansion, and their higher thermal conductivity. The current creep-resistant ferritic steels used in power plants are strengthened by carbides. The creep resistance of those materials decreases in long-term creep tests at temperature over 600 °C, due to the coarsening of the incoherent strengthening carbides [1]. Considerable effort has therefore been made to increase the high-temperature strength of ferritic materials in order to achieve higher operational temperatures and thereby a higher level of efficiency. The approaches that have been followed include a second phase precipitate strengthening. In this respect, the most studied alloy system is the ternary Fe-Al-Ni where there is a miscibility gap between the disordered A2 and the B2-ordered NiAl phases [2,3]; both phases have cubic crystal structure and the mismatch between their lattice parameters is quite small which means that NiAl can precipitate coherently within α-Fe. These NiAl-strengthened ferritic alloys have typical chemical composition based on the pseudobinary section Fe+2.5 at% Al-NiAl+1.25 at% Al with a maximum solvus temperature of 1000 °C that decreases with decreasing volume fraction of the B2 phase [4]. It is known from a long time ago that the NiAl precipitates are effective in increasing the strength of an iron (bcc) solid-solution from room temperature up to 600 °C [5], however, the mechanism of hardening by the NiAl precipitates was quantitatively understood in the recent past [6]. At room temperature the coherent NiAl precipitates were found to be sheared by the ⟨111⟩ slip, which is the primary slip for the bcc matrix, and this shear slip of the precipitates was still active even at 550 °C. Since the creep resistance is one of the most important properties for high temperature applications, the previous research on the Fe-Al-Ni alloy system has also focused on the coarsening behavior of NiAl-type precipitates at high temperatures [7,8] and its relationship with the creep behavior [4,9,10]. Based on these findings,

* Corresponding author. Present address: Gerencia de Materiales, Departamento de Transformaciones y Propiedades, Comisión Nacional de Energía Atómica, Av. Gral Paz 1499, B1650KNA San Martín, Argentina.
E-mail address: rubiolo@cnea.gov.ar (G.H. Rubiolo).

http://dx.doi.org/10.1016/j.msea.2016.12.074
Received 14 October 2016; Received in revised form 16 December 2016; Accepted 17 December 2016
Available online 19 December 2016
0921-5093/

several works have studied the effect of minor alloying elements in order to improve the aforementioned properties of the NiAl-strengthened ferritic steels [4,7,11,12].

Such a miscibility gap also exists in the Fe-Al-V system between the disordered A2 and $L2_1$-ordered Fe_2AlV phases but Fe_2AlV-strengthened ferritic alloys has gained less attention up to now. From the pioneering research of Zhao et al. [13] and Maebashi et al. [14] it is known that this miscibility gap extend roughly in the composition range 5–25 at% Al and 0–25 at% V; it shrinks when the temperature increases up to 750 ºC and then a two-phase equilibrium (B2-ordered Fe(Al,V) + $L2_1$) appears. In a former work [15] we modeled the bcc phase diagram of the Fe-Al-V system by using ab-initio thermodynamics. It was concluded that this ternary system display two kinds of phase separations of the bcc phase, (A2+ $L2_1$) and (B2+ $L2_1$), separate by a tie-line. As the temperature increases this tie-line shrinks and moves toward the Fe-V binary system while its direction remains almost parallel to the line from pure iron to the compound Fe_2AlV. So, any vertical section of the ternary diagram parallel to the section containing the line Fe_{1-2x} Al_x V_x will show the border tie-line parallel to the composition axe. Going from aluminum-rich sections to that of the same composition in aluminum and vanadium, the temperature of the border tie-line increases and the two-phase (A2+ $L2_1$) coherent microstructures could be generated at higher temperatures and with less aluminum content. In order to preserve the idea of designing a Fe_2AlV-strengthened ferritic alloy with good ductility at low temperature, we investigated the $Fe_{1-2x}Al_xV_x$ isopleth with experiments [16]. Fig. 1 shows the experimentally assessed isopleth, phase separation into disordered A2 and ordered $L2_1$ phases occurs for $0.10 < x < 0.15$ at lower temperatures than 720 ºC. Above this temperature and with increasing x in the same range of composition may appear the following regions: (A2+B2), B2 and (B2+$L2_1$). The alloys quenched from 1100 ºC and aged at 700 ºC/2 h show spherical precipitates of $L2_1$ phase for $x \leq 0.13$, for larger values of $x$precipitate coagulation and coalescence is observed [17]. The hardness values, measured at room temperature, for the alloys with $x \leq 0.13$ and ageing temperature between 650 and 700 ºC are comparable to those obtained in the alloy $Fe_{87}Al_{10}Ni_3$ [7]. Recently, the dependence of yield strength with temperature of $Fe_{72}Al_{18}V_{10}$ alloy in the as-cast condition and after heat treatment 700 ºC/1000 h has been investigated by Senčekova et al. [18] with compression test. The flow stress of this alloy, in both heat treated conditions, is even high up to 700 ºC and comparable to those observed for the Fe-Al-Ni alloys with coherent microstructures. These authors have also investigated the creep strength of this alloy between 650 and 750 ºC in the aforementioned heat treated conditions. The dependence of the secondary creep rate with the applied stress measured at 700 ºC predicts a steady-state-creep rate of approximately 10^{-10} s^{-1} at a stress level of 35 MPa which is less but close to the tolerable creep strain rate under operation conditions in fossil-energy power plants [1].

This study has been planned to provide basic information for designing Fe_2AlV-strengthened ferritic alloys for high temperature applications. On this basis, a ferritic $Fe_{76}Al_{12}V_{12}$ alloy was investigated. This alloy composition was chosen to optimize the precipitate volume fraction as well as to avoid precipitate coagulation and coalescence. The coarsening kinetics of Fe_2AlV-type precipitates is examined by the ripening model in multicomponent alloys and its controlling factors of interfacial energy, diffusivities, and alloying element partitioning are discussed. Finally, the increment of strength at room temperature caused by the precipitates was evaluated by precipitation strengthening theory, and the predictions were compared with the experimental data obtained with Vickers micro-hardness test.

2. Experimental procedure

The alloy ingot was melted in an electric arc furnace with tungsten electrode and water cooled copper crucible under argon atmosphere. The purity of the used components was 99.97% Fe, 99.99% Al and 99.7% V. The ingot was then heated in an electric furnace under argon atmosphere up to 1100 ºC and hot rolled in several passes ($\varepsilon < 0.1$) to form a plate with about 3 mm thickness. The average chemical composition of the alloy plate was measured by electron-probe microanalysis in Cameca SX50 equipment. The value was obtained from the average and standard deviation of 50 measurement points along a straight line of 10 mm. Finally, the plate was fractionated by electro-discharge-machining (EDM) in two types of samples: Ø3×3 mm disc shape and 6×8×3 mm cuboid shape.

All the phase transformation temperatures were determined from differential scanning calorimetric (DSC; Setaram LABSYS evo) measurements with heating rate of 5 ºC/min under an argon flow of 25 mL/min. Experiments were carried out with a disc shape sample in alumina crucible. The measurement was made during a heating run after the following conditioning cycle: heating to 1100 ºC, hold for 900 s, cooling to 600 ºC and hold for 600 s.

The short aging treatments (less than 10 h) were performed on the disc shaped samples using the DSC, while for longer aging time we used the cuboid samples and an electric resistance furnace without inert atmosphere. All aging treatments started after a solution heat treatment 1100 ºC /900 s with subsequent cooling to the aging temperature.

The microstructures formed by isothermal ageing were investigated by means of a Transmission Electron Microscope (TEM) (Philips CM200 operated at 160 kV) and the chemical composition of the precipitate phase was analyzed by in-situ Energy Dispersive Spectroscopy (EDS-TEM) (EDAX Apollo X – Philips CM200). To

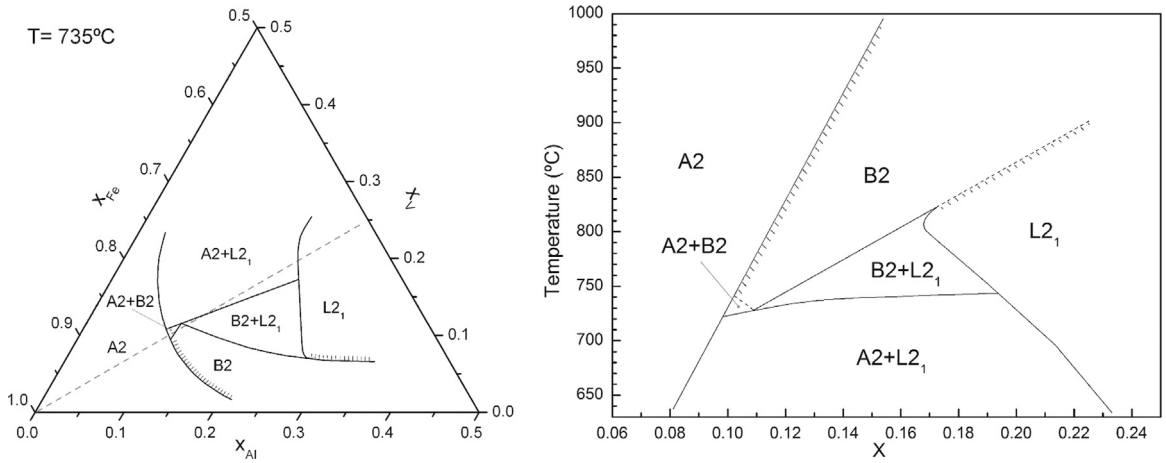

Fig. 1. The experimentally assessed $Fe_{1-2x}Al_xV_x$ isopleth in the Fe rich corner of the Fe-Al-V ternary diagram [16].

minimize contributions to the X-ray intensity spectrum of the underlying matrix in the volume of electron interaction, only the precipitates located at the edge of the holes in the thin films were analyzed. Therefore, the composition values are the average of measurements performed on 5–7 different precipitates. Thin foils for TEM were prepared by cutting 3 mm diameter and 500 μm thickness discs using EDM, mechanically grinding the discs to 100 μm thickness, and final electrolytic thinning of the discs using a double-jet electro polisher STRUERS Tenupol-5 with an electrolyte comprising 67% methanol and 33% nitric acid. Double tilt sample holder was used for TEM observations made mainly with the foil normal in the ⟨110⟩ direction and dark fields images was took in the ⟨200⟩ or ⟨111⟩ directions. Images of the precipitate distributions were captured at different magnifications (21,000× to 205,000×) to obtain a number of precipitates in the range of 100–200. Conventional image analysis software (automatic contrast threshold) was used to isolate and measure each precipitate area from the image pixels. Each measured area determines the radius of a circle of the same area, that radius is taken as the radius of the precipitate.

3. Results and discussion

3.1. The isothermal aging process

The average chemical composition of the alloy measured on the cross section of a hot rolled plate-shaped specimen was Fe 75.83 ± 0.18, Al 11.89 ± 0.15 and V 12.28 ± 0.13 (at%). After heating the alloy up to 1100 ºC and hold it there for 900 s, the DSC results showed that upon heating the alloy undergoes the following reactions sequence: A2→B2; B2→B2+$L2_1$ and B2+$L2_1$→ A2+$L2_1$. The values of the critical temperatures for these reactions are written on the Fig. 2. The identification of these reactions is supported by the results of our previous work on $Fe_{1-2x}Al_xV_x$ alloys [16]. The critical temperatures of the second and third reactions are slightly higher than those estimated from the phase diagram of Fig. 1. The discrepancy is attributed to the longer homogenization time at 1100 °C used during the construction of the phase diagram since the heating rates in the DSC tests were higher [16]. Thus, the highest reliable solvus temperature for the A2+$L2_1$ phase field is that determined from the phase diagram of Fig. 1, ie 720 °C. The alloy quenched from the A2 single-phase field and aged at a temperature below 720 ºC will undergo a homogeneous precipitation of the $L2_1$ phase with morphology of nanosized spherical precipitates. This sets the maximum temperature for the application of this alloy. Another limiting factor is the coarsening of precipitates at high temperatures, which increases the interparticle spacing, thereby reducing the strengthening effect.

Since the Fe_2AlV-strengthened ferritic alloy is proposed by us as

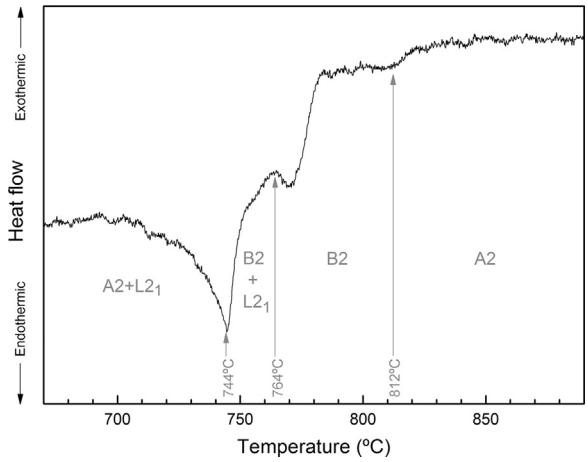

Fig. 2. DSC heating curve (600 ºC → 1100 ºC, 5 ºC/min, argon) of $Fe_{76}Al_{12}V_{12}$ alloy after solution treatment.

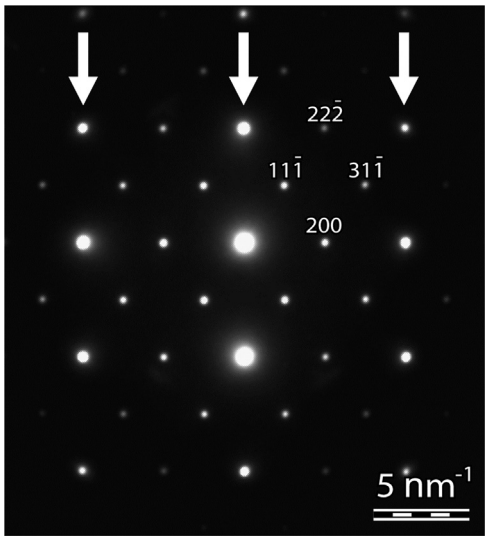

Fig. 3. Alloy aged 22 min at 700 ºC. Diffraction pattern along [011] zone axis indexed corresponding to the $L2_1$-Fe_2AlV structure.

structural material for applications above 600 ºC, then the coarsening kinetics of the Fe_2AlV precipitates was studied in the temperature range 600–700 ºC. The samples were aged for different periods of time ranging from 8 min to 6.5 weeks. The TEM micrographs were used to study the coarsening kinetics of the second-phase particles. A diffraction pattern along the [011] zone axis of an alloy aged by 22 min at 700 °C is shown in Fig. 3. The arrows indicate the rows of reflections where the diffraction of phases A2 and $L2_1$ overlap. The remaining reflections are diffractions coming only from $L2_1$ phase. The shape distribution of precipitates is obtained through the dark field image, coming from a superlattice reflection of the $L2_1$ phase in same sample region, as shown in Fig. 4(a). As can be seen, there are many precipitates reflecting in the same direction. The observations described respect to the diffraction pattern and dark field images confirm that all precipitates have their lattice in orientation relationship parallel to the matrix lattice. Fig. 4(a) and (b) show the dark field image of the $L2_1$ phase morphology at different times during ageing at 700 ºC. A homogeneously distributed and spherical precipitate is observed at every time indicating a coherency between the particle and the matrix, even to large aging times.

3.2. Particle size distributions

The standard microstructural scaling laws that characterize the kinetics of steady-state phase coarsening are established between the precipitate mean radius ⟨r⟩ and the aging time [19–21]. According to the theory of trans-interface diffusion-controlled coarsening (TIDC), developed by Ardell and Ozolins [20, 22], the equation describing the kinetics of growth of the average particle is $\langle r\rangle^n-\langle r_0\rangle^n\approx k\,t$, where r and r_0 are the radii of precipitates at annealing time, t and $t=0$, respectively; n is an exponent ($2\le n\le 3$) related to the width of the matrix-precipitate interface and k is a coarsening constant which is proportional to the interfacial energy and the diffusivity of solute. Additionally, the time exponent n also governs the shape of the scaled particle size distribution (PSD). If the isothermal aging process begins with the supersaturated solid solution, the term $\langle r_0\rangle^n$ can be neglected and a log-log plot of the mean radius of the precipitate against aging time should lead to a linear relationship with a slope of $1/n$. Fig. 5 indicates that the experimental slope is close to the value 1/3 and the k constant increases with increasing temperature. This result in the frame of the TIDC theory means a mechanism of matrix-diffusion-controlled coarsening as modeled in the LSW theory [19].

All the theoretical models which attempt to describe the coarsening

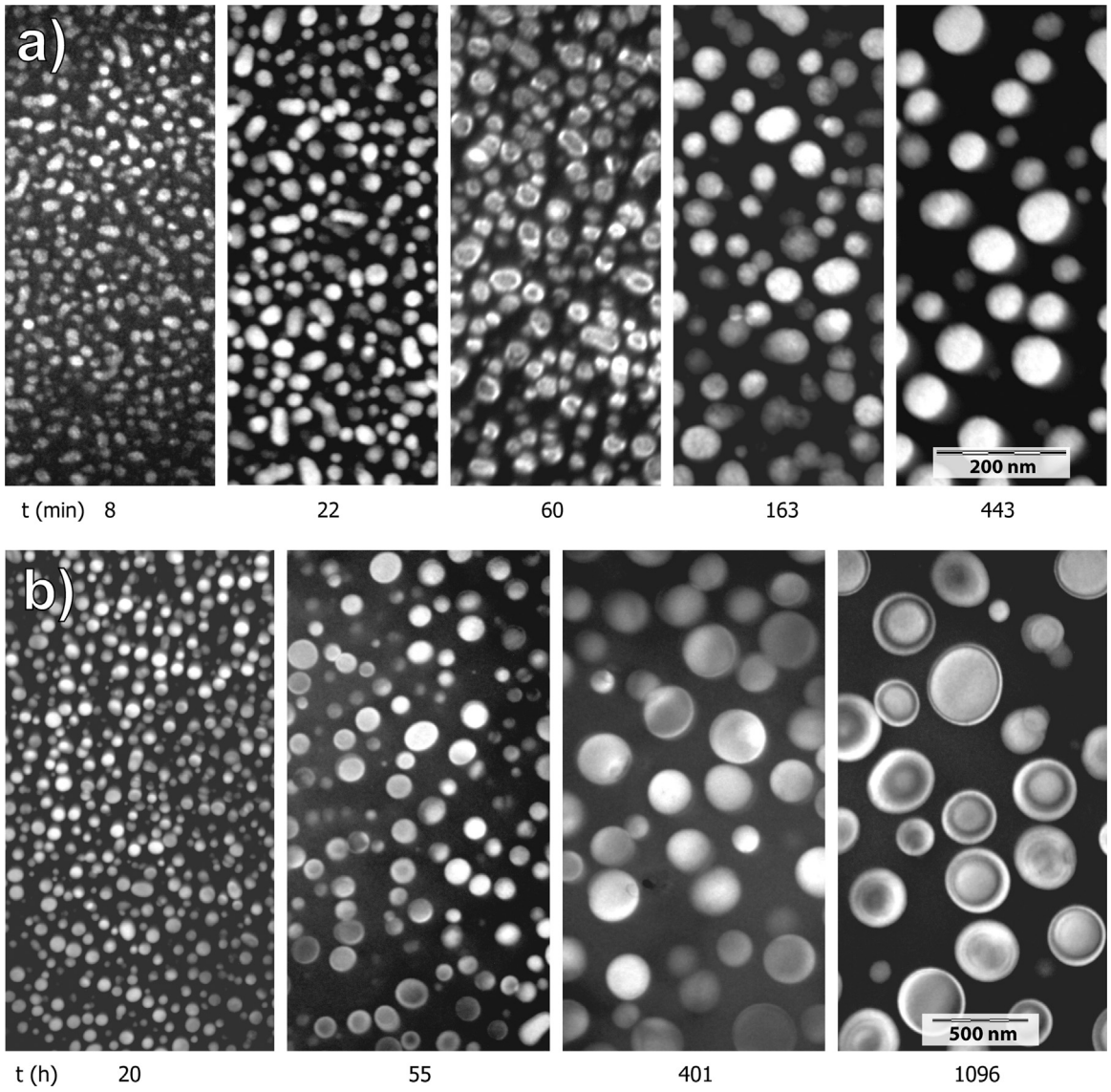

Fig. 4. Dark field TEM image of Fe_2AlV ($L2_1$) precipitates after aging at 700 ºC for different times. (a) Aged in a DSC. (b) Aged in an electric furnace.

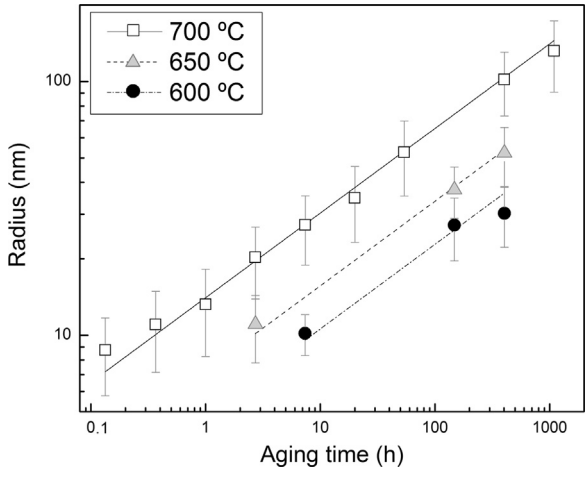

Fig. 5. The growth kinetics of Fe_2AlV precipitates in a $Fe_{76}Al_{12}V_{12}$ alloy for the three aging temperatures indicated. The average precipitate radius is shown together with the error bar calculated as standard deviation of its dispersion.

kinetics of precipitates predict time independent normalized PSD's. Some of the PSD's obtained from measurements in the alloy $Fe_{76}Al_{12}V_{12}$ aged at 700 ºC are given in Fig. 6. The experimental values of the distribution function $g(x)$ are calculated according to the relation:

$$g(x)=\frac{N_i(x,\quad x+\Delta x)}{\sum N_i(x,\quad x+\Delta x)}\frac{1}{\Delta x}$$

where x is the normalized particle radius $r/\langle r\rangle$ and $N_i(x, x+\Delta x)$ represents the number of particles in a given class interval Δx. The prediction of the LSW theory is superimposed on the experimental histograms. At short ageing times, the histogram looks symmetrical as expected for a nucleation phenomenon rather than coarsening of particles. The scaling behavior of the PSD's is observed at sufficiently long aging time, although the distributions are invariably broader than that predicted by the LSW theory. The modification of the LSW theory to include the effect of the precipitated volume fraction, ϕ, on diffusion controlled coarsening kinetics is consistent with the broadening observed in the PSD's of several alloys systems [21,23,24]. In order to know if this effect must be considered in the analysis of our results, we measured (TEM-EDS) the chemical composition of the Fe_2AlV precipitate at the longest times for each aging temperature. The determined values are shown in Table 1 and agree with $L2_1$ solvus

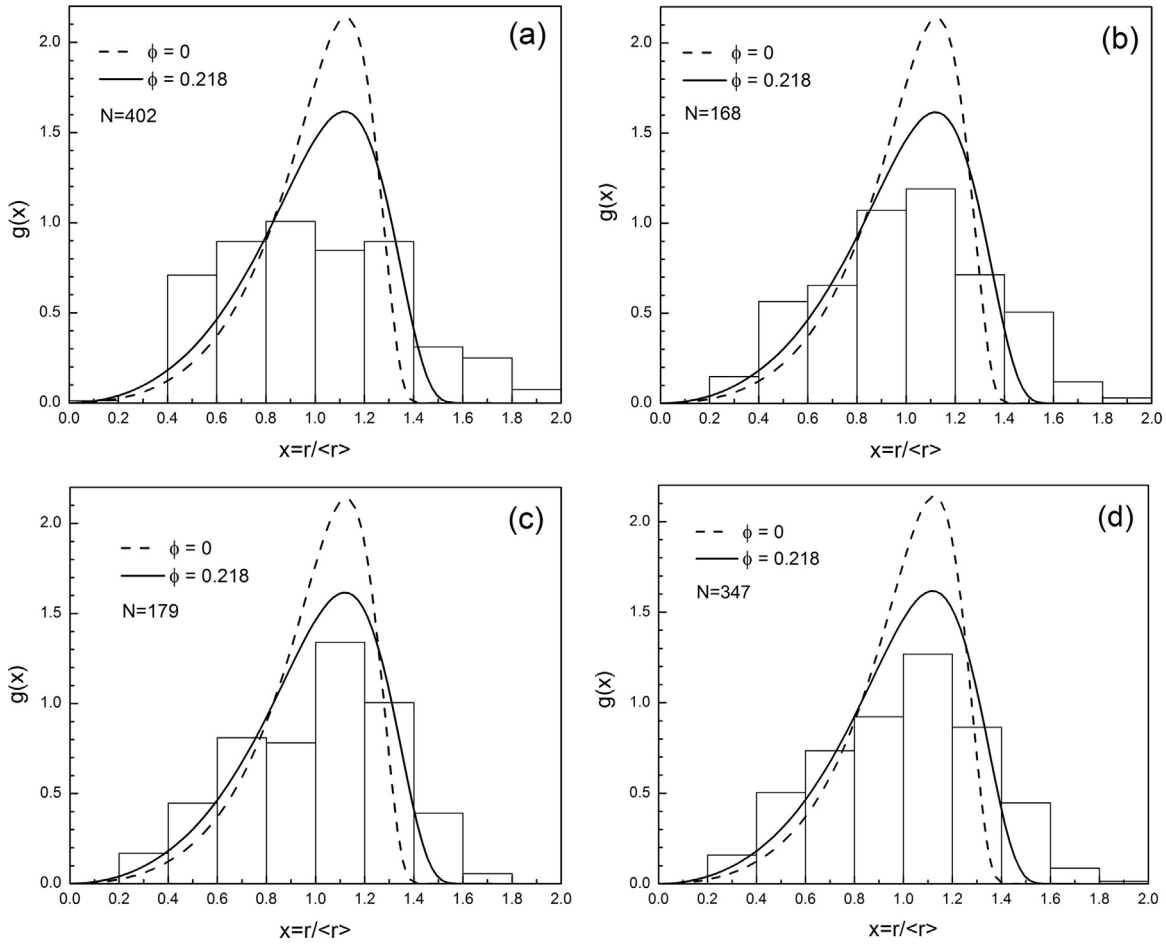

Fig. 6. Particle size distributions for $Fe_{76}Al_{12}V_{12}$ aged at 700 ºC for (a) 0.37 h, (b) 20 h and (c) 1096 h. (d) Cumulative histogram of 20 and 1096 h aging times. The statistical sample size, N, and the equilibrium volume fraction, ϕ, are inset in each plot. The dashed curve represents the PSD computed from the LSW coarsening theory, $\phi = 0$..

Table 1
Equilibrium $L2_1$-precipitate concentration and volume fraction, ϕ, as determined by TEM-EDS and phase diagram of Fig. 1 for $Fe_{76}Al_{12}V_{12}$ alloy aged at different temperatures.

Temperature (ºC)	Time (h)	$\left(\frac{Al+V}{2}\right)$ composition (at%)		Volume fraction
		$L2_1$ precipitate	A2 matrix	$L2_1$ precipitate
600	403	23.3 ± 0.6	7.4	0.284 ± 0.011
650	403	22.6 ± 0.6	8.4	0.249 ± 0.011
700	1096	21.1 ± 0.7	9.4	0.218 ± 0.013

obtained by Maebashi et al. [14]. We can then assume that they have reached their equilibrium composition values and so apply the lever rule to estimate the volume fraction values. The summary of the latest estimated values are also shown in Table 1. In what follows we use these estimated volume fractions in a theoretical model that considers the influence of this variable in the shape of the PSD for the purpose of comparing their predictions with experimental PSD´s.

Numerous attempts have been made over the past 50 years to improve the predictions of coarsening theory by extending its applicability to more realistic (non-zero) volume fractions [21,23,25–29]. These theories consider the effect of nearest neighbors on the growth rate of the precipitates by overlapping their diffusion zones. The challenge is how best to simplify the many-body system, so that a reasonable result is still produced. One method of simplifying such microstructural models to include precipitate-precipitate diffusive interactions, at least to first order, is to replace individual interactions with a cut-off length scale consistent with the mean diffusional flux for a given particle size. It might be thought of as the average distance from the center of each particle in a size class, r, at which the diffusion potential of the particle no longer affects the average potential in the surrounding matrix. A criticism of mean-field coarsening models is the arbitrary specification of this cut-off distance. In what follows we use the model presented in reference [28] where the cut-off distance is identified as a “diffusion screening length", r_D, introduced via the Debye–Hückel theory. Specifically, the diffusion screening length is related to the volume fraction and moments of the microstructure's PSD as:

$$r_D=\left(3 \quad \frac{\langle r\rangle}{\langle r^3\rangle}\phi\right)^{-1/2} \tag{1}$$

showing that the cut-off diffusion distance decreases in inverse proportion to the square root of the volume fraction. This theory provides an approximate relation for grow or shrink rate of the precipitates with radius $r \ll r_D$:

$$\left(\frac{\partial r}{\partial t}\right)=\left(\frac{\partial r}{\partial t}\right)_{LSW}\left(1+\frac{r}{r_D}\right) \tag{2}$$

where $(\frac{\partial r}{\partial t})_{LSW}$ is the growth rate from LSW theory. Eqs. (1) and (2) serves to show that grow or shrink rate of the particles increases for non-zero volume fractions and that the LSW growth rate equation arises as an asymptotic lower limit of the screening model.

Using standard mathematical procedures that are well known in theories of ripening (see Appendix), the diffusion screening coarsening model arrives to the following important predictions needed for the

analysis of our experimental results. These relationships are given in terms of the normalized radius $\rho = r/r_c$, where r_c is a critical radius such that for $r>r_c$ growth and for $r<r_c$ shrinkage of the precipitate occurs:

a. Growth rate of a precipitate of average size

$$\langle r(t)\rangle^3 - \langle r(0)\rangle^3 = K(\phi)\quad t \tag{3}$$

where,

$$K(\phi) = \frac{6\ A}{\rho_{max}^3}\left[2 - \rho_{max}\left(1 - \frac{1}{\rho_D}\right)\right]\langle\rho\rangle^3 \tag{4}$$

The quantity A includes the interface energy γ of the precipitate and an averaged diffusion coefficient as we will discuss later. From Eq. (1) the normalized diffusion screening length, ρ_D, is given by $\rho_D = r_D/r_c = \left(3\frac{\langle\rho\rangle}{\langle\rho^3\rangle}\phi\right)^{-1/2}$. And the dynamically stable maximum-size particle's normalized radius, ρ_{max}, is dependent on the volumetric fraction of the precipitate through ρ_D as $\rho_{max} = 1 - \rho_D + \sqrt{\rho_D^2 + \rho_D + 1}$.

b. The normalized PSD, $G(\rho)$,

$$G(\rho) = \overline{\zeta}\frac{\rho^2 \exp\left[B_4/(\rho_{max}-\rho)\right]}{(\rho_{max}-\rho)^{-B_3}(\rho-\overline{\rho}_5)^{-B_5}} \text{ for } \rho \le \rho_{max}$$

$$G(\rho) = 0 \text{ for } \rho \ge \rho_{max} \tag{5}$$

The roots B_4 and $\overline{\rho}_5$ as well as the exponents B_3 and B_5 are functions of ρ_D and can be taken from reference [21]. The constant $\overline{\zeta}$ is determined by the condition $\int_0^\infty G(\rho)d\rho = 1$.

The PSD in Eq. (5) is scaled by the critical radius. However, the PSD's derived from our experiments are scaled by the average radius. According to the definitions of the average radius and critical radius, one can easily obtain the PSD scaled by average radius in the form

$$g(x) = g(r/\langle r\rangle) = \langle\rho\rangle G(\rho) = \langle\rho\rangle G(\langle\rho\rangle r/\langle r\rangle)$$

To facilitate the comparison between the diffusion screening coarsening theory and our PSD experimental data, the important predicted parameters are tabulated as a function of ϕ in Table 2.

The quantitative analysis of the PSD´s in Fig. 6b) and 6c) is highly restricted by the sample size, which varied between 168 and 179 particles. A statistically reliable PSD requires the use of a much higher number of particles. Regardless of aging time, however, the experimental PSD´s remain similar in their appearance suggesting that coarsening is the predominant mechanism. Then, we can consider that the steady-state was reached in samples aged for 20 h or longer. If so, the cumulative histogram of Fig. 6d) is a more accurate representation of the experimental PSD. There is shown that the observed breadth and generally symmetrical form of the experimental PSD correlates better with the PSD calculated from diffusion screening coarsening theory than from LSW theory.

As can be seen in Table 2, the aging temperature changes the volume fraction of precipitates by 30% but the predicted parameters from the theory for the PSD's are weakly affected. This effect is observed in the experimental PSD's shown in Fig. 7a) and b) where the aging time at each temperature was long enough to assume that the temporal stability of the PSD was reached. As small changes are expected in the theoretical PSD´s for the aging temperature range investigated, all the normalized radii taken from the individual histograms at the different temperatures and times of aging were combined to obtain the cumulative histogram of Fig. 7c) with a total count of 575 particles. This large number of samples provides confidence in our assertion that the height and width of the PSD including the largest radius of the dynamically stable precipitates measured in the microstructure, ρ_{max}, are accurately predicted with the diffusion screening coarsening theory.

3.3. Kinetics

The diffusion screening coarsening theory predicts the kinetics of steady-state phase coarsening with Eqs. (3) and (4). In Fig. 5 the precipitate mean radius ⟨r⟩ and the aging time measured in our experiments for three different temperatures is drawn in a log-log plot. As was discussed before, linearity of this kinetic relationship is indeed observed with a fixed slope of 1/3. Linear regression was used to fit these data with that fixed slope, the intercepts corresponds to $\{(1/3)\log K(\phi)\}$ from where the experimental coarsening rate constant $K(\phi)$ can be calculated. Then, using the values of ρ_{max}, ρ_D and $\langle\rho\rangle$ from Table 2 into the Eq. (4), we can estimate the constant A as shown in Table 3.

The A constant for the temporal evolution of the precipitate radius in a ternary alloy is given by [30]

$$A = \frac{\gamma V_m}{\Lambda} \tag{6}$$

where $V_m = 7.196\times10^{-6}$ m^3/mol is the average atomic volume per mol of the Fe_2AlV phase, deduced from $V_m = N_a a^3/16$ (N_a is Avogadro's number, a=0.5761 nm is the lattice parameter of Fe_2AlV [31]), γ is an average interfacial energy. The coefficient Λ is given by

$$\Lambda = \frac{\Delta C_{Al}}{D_{Al}}(\Delta C_{Al}G''_{AlAl} + \Delta C_V G''_{AlV}) + \frac{\Delta C_V}{D_V}(\Delta C_{Al}G''_{AlV} + \Delta C_V G''_{VV}) \tag{7}$$

where $\Delta C_i = C_i^\beta(r) - C_i^\alpha(r) \approx C_i^\beta(\infty) - C_i^\alpha(\infty)$; $C_i^{\alpha/\beta}(r)$ and $C_i^{\alpha/\beta}(\infty)$ are the concentrations in the α- and β-phases (matrix and precipitate phases) near and far from the precipitate interface respectively. This approximation implies that a possible enhancement of solute concentration at the curved interface is negligible in the evaluation of the ΔC_i. The G''_{ij} are the second derivatives of the Gibbs free energy with respect to the concentrations of i and j, with i, j= Al, V; the D_i are the diffusion coefficients of Al and V in the cubic (bcc) α-(Fe, Al, V) disordered matrix. Assuming the matrix phase is described by dilute ideal solid-solution theory, the derivatives of the Gibbs free energy are given by

$$G''_{AlAl} = \frac{RT[1-C_V^\alpha(\infty)]}{C_{Al}^\alpha(\infty)[1-C_{Al}^\alpha(\infty) - C_V^\alpha(\infty)]} \tag{8}$$

$$G''_{AlV} = \frac{RT}{[1-C_{Al}^\alpha(\infty) - C_V^\alpha(\infty)]} \tag{9}$$

$$G''_{VV} = \frac{RT[1-C_{Al}^\alpha(\infty)]}{C_V^\alpha(\infty)[1-C_{Al}^\alpha(\infty) - C_V^\alpha(\infty)]} \tag{10}$$

Since in our alloy $Fe_{76}Al_{12}V_{12}$ was shown that $C_{Al}^\alpha \approx C_V^\alpha$ and $C_{Al}^\beta \approx C_V^\beta$ (see Fig. 1 and Table 1) results $\Delta C_{Al} = C_{Al}^\beta - C_{Al}^\alpha \approx C_V^\beta - C_V^\alpha = \Delta C_V$ and the Eqs. (6–10) simplify to give

$$A = \frac{\gamma V_m C_{Fe}^\alpha C_{Al}^\alpha}{RT(\Delta C_{Al})^2(C_{Fe}^\alpha + \ 2\ \ C_{Al}^\alpha)}\left(\frac{D_{Al}D_V}{D_{Al}+D_V}\right) \tag{11}$$

Assuming that the interfacial free energy does not vary with aging temperature, i.e. γ remains constant in Eq. (11), the activation energy

Table 2
The predicted parameters in the diffusion screening coarsening theory for the PSD experimental data.

T (°C)	ϕ	ρ_D	ρ_{max}	$\overline{\rho}_5$	B_3	B_4	B_5	$\langle\rho\rangle$
600	0.284	1.08 ± 0.02	1.721 ± 0.001	−0.925	−4.654	−3.358	−1.382	0.966
650	0.249	1.16 ± 0.03	1.712 ± 0.002	−0.978	−4.605	−3.272	−1.407	0.973
700	0.218	1.24 ± 0.04	1.704 ± 0.003	−1.031	−4.593	−3.188	−1.442	0.983

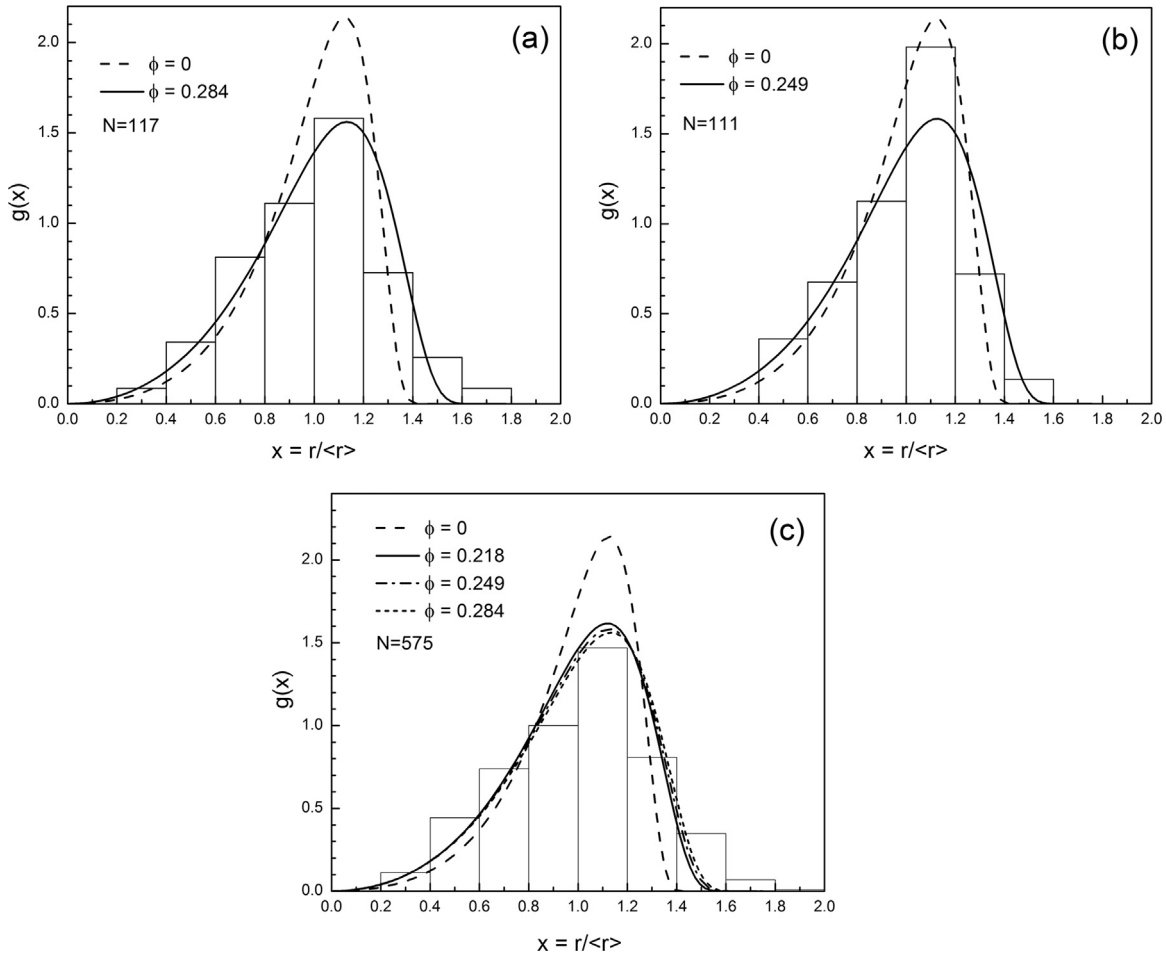

Fig. 7. Particle size distributions for $Fe_{76}Al_{12}V_{12}$ aged at: (a) 600 ºC for 403 h, (b) 650 ºC for 148 h. (c) Cumulative histogram of the histograms from Fig. 6b), 6c), 7a) and 7b). The curves represent the PSD's computed from the diffusion screening coarsening theory with the parameters of Table 2.

Table 3
The measured coarsening constants ($K(\phi)$ and A) for the $Fe_{76}Al_{12}V_{12}$ alloy for three different temperatures; the diffusivity of Al and V in ferromagnetic (bcc) α-Fe; and the estimated interfacial energy of the Fe_2AlV ($L2_1$) precipitates in the ferritic matrix.

T (ºC)	ϕ	$K(\phi) \times 10^{-2}$ (nm^3/h)	$A \times 10^{-1}$ (nm^3/h)	$\widetilde{D}$ (m^2/s)	$\gamma \times 10^{-3}$ (J/m^2)
600	0.284	1.18 ± 0.11	5.95 ± 0.65	2.88×10^{-20}	232 ± 43
650	0.249	3.86 ± 0.17	19.8 ± 1.4	3.77×10^{-19}	45 ± 7
700	0.218	27.9 ± 1.1	145 ± 10	4.53×10^{-18}	18 ± 3

for coarsening can be obtained by plotting $log\left(\frac{(A\,T)(\Delta C_{Al})^2(C^{\alpha}_{Fe}+2C^{\alpha}_{Al})}{C^{\alpha}_{Fe}C^{\alpha}_{Al}}\right) vs\, 1/T$. By doing this we get an activation energy value of $(174 \pm 33) kJmol^{-1}$. The diffusion of several solutes in α-Fe [32–35] show a linear Arrhenius plot in the paramagnetic region but a break at the Curie temperature (T_C=770 ºC) and a soft upward curvature at lower temperatures in the ferromagnetic region, these values being lower than the ones extrapolated from the high temperature region. In order to model this effect the expression for the diffusion coefficient in a ferromagnet is given by [36]

$$D = D_0 exp\left[-Q_p(1+\eta s^2)/RT\right] \quad (12)$$

where Q_p is the activation energy for diffusion in a paramagnetic state, s is the ratio of the spontaneous magnetization at temperature T to that at 0 K (reduced magnetization) and has been experimentally determined by Crangle and Goodman [37] and the value of ηQ_p seems to be around 0.4 eV for all the measured elements except Co. The Curie temperature (T_C) of the α-Fe phase has been measured as a function of composition in the Fe-Al [38] and Fe-V [39] systems, there is agreement that V additions to Fe cause the T_C of the α-Fe to pass through a maximum near 840 ºC and between 13 and 14 at% V, instead of this, the addition of Al decreases the T_C continuously. Both effects evaluated for the $Fe_{76}Al_{12}V_{12}$ composition suggest that the T_C remains close to that of pure α-Fe phase, so the diffusion process that leads to coarsening of the Fe_2AlV ($L2_1$) precipitates in our aging experiments takes place in a ferromagnetic matrix. The known experimental Al and V diffusion data in pure paramagnetic α-Fe are fitted to a Arrhenius expression with the following constants [40]: $D_0^{Al}=5.35\times10^{-4} m^2 s^{-1}$; $Q_p^{Al}=241 kJmol^{-1}$; $D_0^{V}=124\times10^{-4} m^2 s^{-1}$; $Q_p^{V}=274 kJmol^{-1}$. It is easy to see from Eq. (11) that $\widetilde{D}$ should be dominated by the slower diffuser, ie vanadium. In Table 3 is shown the diffusivity of Al and V in ferromagnetic (bcc) α-Fe given by $\widetilde{D}=\{D_{Al}D_V/(D_{Al}+D_V)\}$ and calculated by using all these information. Remarkably, the obtained value of the activation energy for coarsening is much lower than the activation energy associated to $\widetilde{D}$ in Table 3. At first glance it can be argued that this discrepancy comes from not considering the high alloying content on the diffusivity of Al and V. Efforts have been made in the past [41–43] to combine experiments and modeling to determine the diffusivity values of Al and other solutes (Co, Ni, Cr, Mn, Zn, and In) in concentrated, ordered or disordered Fe-Al alloys. Reliable values are still unavailable for Al diffusivity in the disordered A2 matrix for aluminum concentrations lower than 20 at%. However, the value reported in reference [41] for D_{Al} at 1000 °C and 17 at% Al shows that aluminum diffusion is faster by about a factor two respect to its diffusion in pure bcc iron. Another important result for

our analysis can be obtained from the reported results of the diffusion of solutes in the disordered alloy with Fe_3Al composition [42]. There it can be seen that the solute which substitute on the Al sublattice (Zn, In, Cr, Mn) diffuse with similar rates as Al, while the solute that substitutes in the sublattice of Fe (Co, Ni) diffuses more slowly than when they diffuse into pure bcc iron. Vanadium substitutes in the sublattice of Fe to form the Heusler phase Fe_2AlV, the precipitate whose coarsening we are investigating. Given this background for the diffusivity values of Al and other solutes in concentrated disordered Fe-Al alloys, the activation energy for coarsening should be equal to or greater than the activation energy for vanadium diffusion in pure bcc iron refusing the experimental result obtained with the hypothesis that the interfacial free energy is independent of the aging temperature. Then, we propose that the interfacial energy can be temperature dependent and, in the lack of reliable experimental values for the concentrated alloys of Fe-Al, we evaluate this hypothesis using the diffusivity of Al and V in pure bcc iron.

The interfacial energy at each ageing temperature was then evaluated from Eq. (11) and the values in Table 1. As can be seen in Tabla 3 the estimated interfacial energy is strongly temperature dependent. These energies drop rapidly with increasing temperature falling to $\sim 20\ mJ\ m^{-2}$ at 700 ºC which is within the range of the limited measurements based on growth kinetics of NiAl precipitates in ferritic Fe-Al-Ni alloys [7]. In ours coarsening experiments, as shown in Fig. 3, the precipitate has the same crystal structure and a similar lattice parameter to the matrix phase and the two lattices are in parallel orientation relationship. This means that the two crystal structures match more o less perfectly across all interfacial planes so the precipitate can be any shape and remain fully coherent. The spherical form of the observed precipitates only indicates that there is a crystalline isotropy of the interface energies in the α-Fe(Al, V)/Fe_2AlV system, particularly for low-index boundaries whose interfacial energy accounts for the interatomic forces between first and second neighbors at the interfacial plane separating two cubic crystalline phases [44]. Hence, an average of the interfacial energies of low-index boundaries should be a good approach to the estimated interfacial energy values in Tabla 3. Recently, it was found through independent first-principles studies that the average of the interfacial energies of low-index boundaries in the Ni–Ni_3Al system behave with temperature like shows the trend of our results [45]. The main results of these studies show that in the low-temperature sharp interfacial boundary the spin moments evolve smoothly over 2–3 atomic layers and this spin density transition across the boundary is the main contribution to the interfacial energy; as the temperature rises the interfacial boundary becomes disordered and diffuse, so its configurational entropy increases and acts to reduce the interfacial free energy.

3.4. Precipitation strengthening and deformation mechanisms at room temperature

The hardness curves of Fig. 8 reflect the precipitation process occurring in the $Fe_{76}Al_{12}V_{12}$ alloy during aging in the two-phase region A2+ $L2_1$ of the Fe-Al-V phase diagram. The results are comparable with our previously published hardness values for $Fe_{1-2x}Al_xV_x$ alloys [16]. The average hardness value of our specimens after homogenization and quenching (but before aging) is 312 ± 19 HV and they have a B2 ordered phase displaying antiphase domains boundaries (APB) due to the A2 disordered structure present at high temperatures could not be retaining by quenching as the order-disorder transformation A2→B2 of the system (see Fig. 1) have a very high transformation speed and the ordering reaction start during cooling. This hardness value is close to that of the iron-rich B2 FeAl alloys [46,47] which strengthening mechanism was associated to the interaction of moving dislocations with retained vacancies sites from water-quenching [48]. As was observed with the hardness of the Ni-doped B2 FeAl alloys where no conclusive evidence of solute hardening by Ni itself was found [49], the role of V in the hardening of V-doped B2 FeAl alloys appears to be restricted to the influence of these V additions on the vacancy concentration.

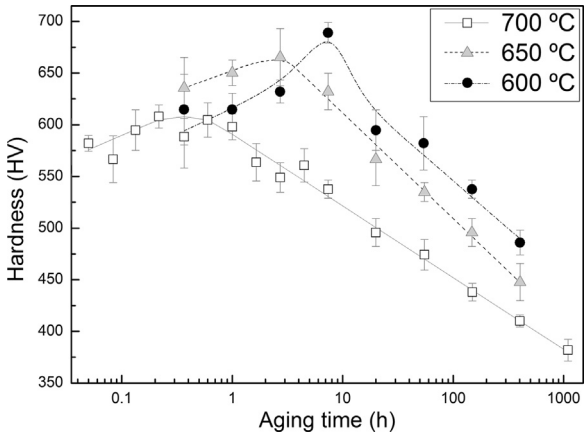

Fig. 8. Vickers microhardness evolution during isothermal aging of the $Fe_{76}Al_{12}V_{12}$ alloy.

The aging response of the alloy exhibits three different regions (Fig. 8): (a) a transient period with a rapid increase in hardness values; (b) a plateau at high hardness values (peak aging); and (c) a slow decrease of the hardness. As the aging temperature increases from 600 to 700 °C, the time to reach the peak hardness and its value decreases, and the rate of hardness drop after peak aging seems to be constant. By comparing results in Figs. 5 and 8, it should be noted that the peak hardness at 700 ºC is achieved when the precipitate coarsens. The absence of observable incubation time in the ageing process at 700 ºC can be attributed to the very rapid nucleation rate due to the high supersaturation, low strain energy and low interface energy. In what follows we assume that this hypothesis holds also for aged alloy below 700 °C. By comparing the same set of results it can be done another important observation, peak hardening is achieved with roughly equal size of precipitate (~10*nm*) and its strength increases as does the volume fraction of the precipitates (see Table 1). These last findings are in agreement with the theory of precipitation strengthening due to the shear of a coherent ordered particle by a matrix dislocation presented by Hüther and Reppich [50–52] even though we have no experimental evidence. However it was reported in early studies of NiAl-B2 strengthened $Fe_{71}Al_{23}Ni_6$ [6] and $Fe_{77}Cr_{20}Ni_2Al_1$ [53] ferritic steels that, up to peak strength, the precipitates are essentially sheared by screw dislocations which are found to be grouped in pairs as supposed in the Hüther-Reppich (HR) model. Because both B2 and $L2_1$ phases precipitate in the matrix of α-(Fe, Al) satisfying the same relation cube-on-cube with small misfit strain, we expect the same order strengthening mechanism operating in the $Fe_{76}Al_{12}V_{12}$ alloy.

For a comparison with the proposed theoretical model of particle strengthening it is more appropriate to plot the experimental data of Fig. 8 in terms of the increase in critical resolved shear stress (CRSS), $\Delta\tau_p$, as a function of the average precipitate radius (Fig. 9). Therefore, we estimate $\Delta\tau_p$ for every aged conditions with the equation $\Delta\tau_p \approx (1/3M)(\sigma_{ys}^H - \sigma_0^H)$ where M is the Taylor factor (approximately 2.9 for bcc materials [54]) and the yield stress is estimated using the equivalent maximum pressure σ^H obtained from the Vickers microhardness measurements of Fig. 8 and the Tabor's empirical relationship [55] $\sigma^H \approx 3\sigma_{ys}$. In the literature an appropriate value for σ_0^H is usually taken from the yield stress of the solution annealed material. However, as it was discussed before, we were not successful to produce an A2 single phase solid solution by quenching. Alternatively, we used a value of $\sigma_0^H = (2.4 \pm 0.1) GPa$ obtained from the alloy $Fe_{84}Al_8V_8$ in our previous work on the characterization of $Fe_{1-2x}Al_xV_x$ alloys [16] because of its similarity in chemical composition with the matrix of the $Fe_{76}Al_{12}V_{12}$ alloy during precipitation (see Fig. 1).

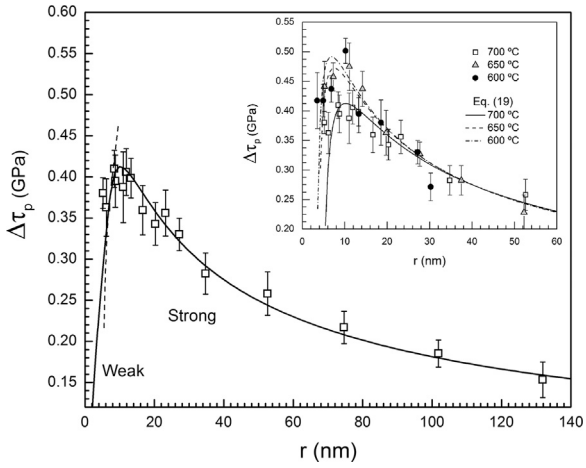

Fig. 9. The CRSS increase as a function of the average precipitate radius. Same symbolism as in Fig. 8.

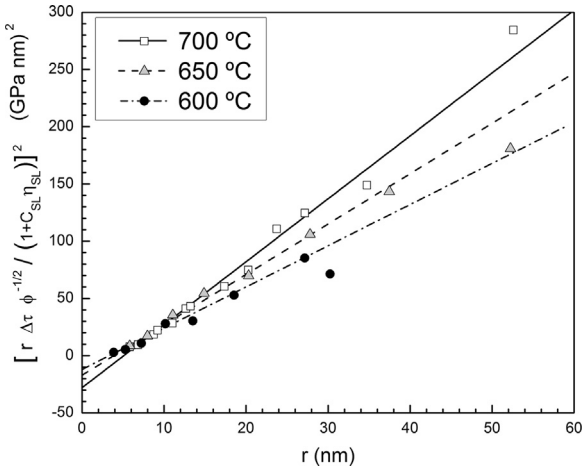

Fig. 10. Measured CRSS increment of aged $Fe_{76}Al_{12}V_{12}$ as a function of the mean particle radius represented as $\{r\,(\phi^{-1/2})\,\Delta\tau/[1+C_{SL}\eta_{SL}]\}^2$ vs r according to the HR formula, Eq. (16). Straight lines are the estimates through the least squares method.

Following the proposed hardening model, we postulate that at room temperature the overcoming of ordered Fe_2AlV particles in a disordered metallic matrix occurs by dislocation pairs creating an antiphase domain boundary (APB) of energy γ_{APB}. Fine under-aged dispersions of these particles are considered to be cut by weakly pair-coupled dislocations giving an increase in CRSS according to [52]

$$\Delta\tau_{weak}=\left[\left(\frac{\gamma_{APB}}{b}\right)^{3/2}\left(\frac{br\phi}{2\ T}\right)^{1/2}A-\ \ \frac{\gamma_{APB}\phi}{2\ \ b}\right]\times[0.\ 94\times(1+C_{SL}\eta_{SL})] \tag{13}$$

where C_{SL} and η_{SL} represent an empirical constant and the normalized particle depth in the theory of Schwarz and Labusch [56], r is the mean particle radius, $A=0.72$ for spherical particles, T is the dislocation line tension and b its Burgers vector. For larger particle sizes strong pair-coupling applies and the increase in CRSS is modified according to Hüther and Reppich [57]

$$\Delta\tau_{strong}=\left[\frac{1}{2}0.\ 83\frac{wT\phi^{1/2}}{br}\left(\frac{\pi^2}{4}\frac{\gamma_{APB}r}{wT}-1\right)^{1/2}\right]\times[0.\ 94\times(1+C_{SL}\eta_{SL})] \tag{14}$$

with the constant w accounting for the elastic repulsion between the strongly paired dislocations and is a fitting parameter. Finally, beyond a critical radius the particles may be overcome by Orowan by-passing since the Orowan stress becomes smaller than the 'cut-in' stress. A critical review of Kocks [58] suggested the following best formula for the Orowan-stress:

$$\Delta\tau_{Or}=0.\ 9\ \ \times\frac{[\ln(2\pi r/b)]^{3/2}}{[ln(L/b)]^{1/2}}\times\frac{K^{dipole}}{b[L-(\pi/2)r]} \tag{15}$$

which considers all further effects of the extended width of impenetrable obstacles, such as: the center-to-center square lattice spacing $L=\left[(2\pi/3\phi)^{\frac{1}{2}}\right]r$ and the interparticle spacing $[L-(\pi/2)r]$; the statistical distribution in the glide plane and the elastic dipole interaction K^{dipole} of the dislocation segments near the particles [59].

Several other assumptions, taking data from literature, ought to be made in order to compare the experimental results with theoretical calculations. The lattice parameter, a, and Young modulus, E, of the matrix were taken from data for the α-Fe(Al) disordered solid solution at x_{Al}=0.16 considering that the composition of the matrix is that of alloy $Fe_{84}Al_8V_8$ and V atoms behave like Al atoms, then $a=0.2885nm$ [60] and $E=163GPa$ [61]. The Poisson modulus ν was set at 1/3 and the shear modulus was evaluated as $G=E/[2(1+\nu)]$. Because most active slip systems in the bcc structure occur on any plane containing a ⟨111⟩ direction, the length of the Burgers vector of the bcc matrix is taken as $b=(a/2)\langle111\rangle$=0.2498nm.

The course of the data points in Fig. 9 exhibits mainly the functional dependency predicted by Eq. (14), namely a distinct maximum and then a gradual hyperbolic decrease for overaged particles in the HR regime [51]. The whole relationship can be checked by plotting $[r\,\Delta\tau\,\phi^{-1/2}/(1+C_{SL}\eta_{SL})]^2$ vs r (see Fig. 10). The Schwarz and Labusch correction term was estimated by using C_{SL}=3 and $\eta_{SL}=(\phi^{1/2}/2)$ as suggested by Reppich et al. in their analysis of the room temperature yielding of the Ni-based alloy Nimonic PE16 containing monodispersed, randomly spaced and spherical γ' precipitates [62]. In Fig. 10 data points follow a straight line as qualitatively expected from the coordinate transformation applied to Eq. (14):

$$[r\,\Delta\tau\,\phi^{-1/2}/(1+C_{SL}\eta_{SL})]^2=\left[\left(\frac{0.94\times0.83\times\pi}{4}\right)^2\frac{w\ T\ \gamma_{APB}}{b^2}\right]r-\left(\frac{0.94\times0.83}{2}\frac{w\ T}{b}\right)^2 \tag{16}$$

The linear regression to fit Eq. (16) to the data in Fig. 10 gives the opportunity to estimate the APB energy γ_{APB} and the amount $(w\,T)$ whose factors are the dislocation line tension and the elastic repulsion between the strongly paired dislocations. The best estimated values of these quantities are shown in Table 4 for each aging temperature. Then, the calculated curve by placing these values into Eq. (14) was drawn on the insert of Fig. 9. The fitting value of γ_{APB} is stable and in excellent agreement with the values obtained by first principles calculations of $(a/2)\langle1\bar{1}\bar{1}\rangle(01\bar{1})APB$ in Fe_2AlTi and Fe_2AlNb intermetallic at 227 °C [63]. An average elastic repulsion between the strongly paired dislocations, $w=3.42\pm0.16$, was estimated from the junction of both curves given by Eqs. (13) and (14) at each temperature. The procedure is displayed in Fig. 9 for the curves at 700 °C. With this estimate we can obtain the values of the dislocation line tension at each temperature as is written in Table 4. The CRSS according to Eq. (14) has its maximum at $r_{ws}=(8w\,T)/(\pi^2\gamma_{APB})$ and it indicates the transition from "weak" to "strong" pair-coupling (index *"ws"*); the calculated values of r_{ws} are also given in Table 4. As can be seen both T and r_{ws} decrease as the volume fraction of precipitates increases.

Table 4
The estimates of the APB energy of the Fe_2AlV ($L2_1$) precipitates, the transition radius r_{ws} from "weak" to "strong" pair-coupled dislocations and the line tension T of the leading dislocation bowed between the particles in the ferritic $Fe_{76}Al_{12}V_{12}$ alloy.

T (°C)	ϕ	γ_{APB} (J/m^2)	wT (GPa nm^2)	T (GPa nm^2)	r_{ws} (nm)
600	0.284	0.27 ± 0.03	2.22 ± 0.08	0.65 ± 0.05	6.7 ± 1.2
650	0.249	0.28 ± 0.04	2.64 ± 0.09	0.77 ± 0.06	7.6 ± 1.4
700	0.218	0.27 ± 0.04	3.39 ± 0.24	0.99 ± 0.12	10.2 ± 1.9

No discussion of this topic can be complete without mention of the role of the character of the dislocations on the CRSS. In reality the line tension of a curved dislocation depends on the angle between the dislocation line and its Burgers vector [64], so the dislocation shape is not truly circular as it bows out between two obstacles. Instead, its radius of curvature or local tension line is changing at every point on the line. Then, the equilibrium condition of the curved dislocation under an applied stress can be obtained through of an average line tension calculated over the length of the arc. In the more general case that the orientation dependence of the line energy is given by isotropic elasticity theory, the extreme values of the average line tension, $\langle T \rangle$, namely those applicable to a dislocation that starts out either as a pure screw or as a pure edge, can be derived to be [65,66]:

$$\langle T_{edge} \rangle = \kappa \{1 + \nu - 3\nu[1 - (sin^2(\theta_c/2))/3]\}/(1 - \nu) \quad (17)$$

$$\langle T_{screw} \rangle = \kappa [1 + \nu - \nu (sin^2(\theta_c/2))]/(1 - \nu) \quad (18)$$

where $\theta_c/2$ is the bow-out angle and

$$\kappa = \frac{G\, b^2}{4\,\pi} \ln\left(\frac{\Psi}{b}\right) \quad (19)$$

A further problem in applying Eqs. (17) and (18) is the choice of the outer cut-off radii, Ψ, in Eq. (19) because it should reflect the fact as the dislocation bows out more when the obstacle strength increases, the attractive interaction between adjacent arms at the obstacle is also stronger and thereby tending to reduce $\langle T \rangle$. This issue was discussed by several authors reaching similar results [51,61,67]; we use here the proposal given by Reppich for order hardening [51]:

$$\Psi = \left(\frac{4 \quad \pi\langle T \rangle}{3 \times 0.8 \quad \phi\gamma_{APB}}\right)^{1/2} r^{1/2} \qquad r < r_{ws}$$

$$\Psi = \left(\frac{2 \quad \pi}{3 \quad \phi}\right)^{1/2} r \qquad r > r_{ws}$$

Fig. 11 shows the prediction of the normalized average line tension, $2\langle T \rangle/\kappa$, versus the bow-out angle as obtained from Eqs. (17) and (18) together with the same value calculated from the experimental fitting parameters given in Table 4 and the outer cut-off radii, Ψ, calculated for $r = r_{ws}$. The comparison let see that the glide dislocations should have a mix character with a small screw component and, as expected, dislocations bows out more with increasing the precipitate radius and decreasing the volume fraction.

The Orowan process can be observed only in our data at 700 ºC

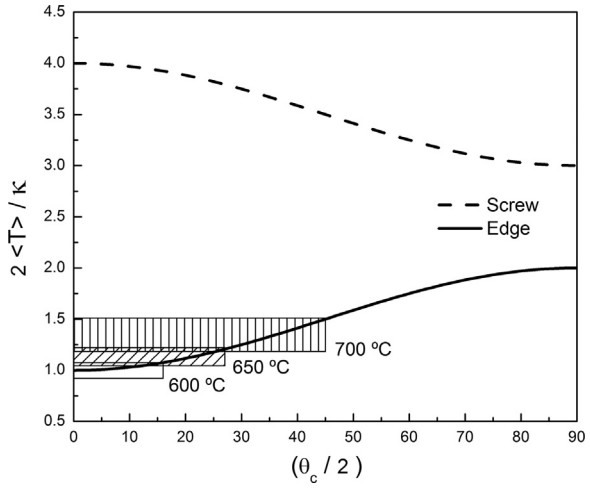

Fig. 11. Theoretical dependence of the average line tension $\langle T \rangle$ for an initial screw and an initial edge dislocation on the bow-out angle $\theta_c/2$ and it comparison with the fitting values of Table 4 (see text). The rectangular band takes into account the different error values of $\langle T \rangle$.

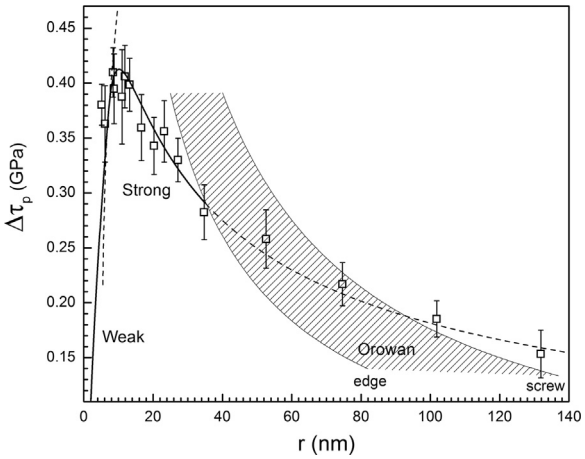

Fig. 12. The transition from cutting to Orowan looping in the $Fe_{76}Al_{12}V_{12}$ alloy aged a 700 ºC. The Orowan stress of Eq. (15) is presented as a curve band which accounts for different dislocation character.

because the radius range is enough extended. The Orowan stress, defined by Eq. (15), is presented in Fig. 12 as a curve band, which accounts for different dislocation character. It should be noted that the transition from strong pair-coupled cutting to Orowan looping of non-coupled single dislocations can be certainly expected to occur starting at a critical radius of $r \approx 35nm$ if the gliding dislocations had net edge character, however, a deviation from the predicted hyperbolic decrease towards the higher Orowan stress for screw dislocations is visible indicating that a transition in the mix character of the involved dislocations occurs over a large radius range. Of course, this transition also involves the statistical character of the distribution of precipitate size and inter-particle spacing.

The theoretical predictions for the controlling mechanism of the dislocation particle interaction should be verified by TEM observation of deformed specimens; however, we cannot do that with our specimens after Vickers hardness test. In order to provide this experimental evidences we have under way mechanical compression test at 600 ºC in samples aged at 700 ºC for suitable times.

4. Conclusions

A study has been made on the coarsening process of Fe_2AlV precipitate in the $Fe_{76}Al_{12}V_{12}$ alloy aged between 600 and 700 ºC as well as the strengthening mechanism of the alloy by the precipitate at room temperature. The following conclusions were drawn:

A linear relationship between the precipitate mean radius and one third root of the aging time is well satisfied, which is consistent with a mechanism of matrix-diffusion-controlled coarsening.

Good agreement is found between the diffusion screening coarsening theory and experiment regarding the shape of the precipitate size distribution when the aging time at each temperature was long enough to assume that the temporal stability of the PSD was reached.

The coarsening rates were determined at 600, 650 and 700 °C; the consistency between the experimental results and theoretical predictions from the diffusion screening coarsening theory, taking into account the mobility of the components in the ternary alloy, provided a way to estimate the interfacial energy between the two phases. We found that interfacial energy is strongly temperature dependent but, the spherical morphology of the precipitates remains essentially unaltered suggesting that coherency strains may not be a controlling factor of the interfacial energy. Therefore, based in previous first principles studies done for others authors, we suggested that the interfacial energy is dominated by the Fe spin density transition across the interfacial boundary and its behavior with temperature is due to the ferromagnetic ordering effect in the ferritic matrix.

A classic precipitation hardening behavior has been observed along the time for each aging treatment. The coherent Fe_2AlV precipitates increase the room-temperature flow stress of the ferritic matrix for about 450 MPa. The precipitate radius corresponding to peak strengthening is about 10 nm. The peak strengthening increases with increasing volume faction of precipitates. Quantitative agreement is found with strength values predicted from order strengthening theory, predicting that strength is controlled by a precipitate shearing mechanism for sizes around that of peak strengthening, and the Orowan dislocation bypass mechanism for larger sizes. The APB energy of Fe_2AlV precipitate was estimated to be $(27 \pm 4)\times 10^{-2} J/m^2$. When the shearing mechanism is operating the dislocations have a mixed character with a strong edge component and they are grouped in pairs. The Orowan process is carried out with mixed dislocations whose main component changes from edge to screw character with increasing radius of the precipitate.

Acknowledgments

The authors thank the heads of the research groups belonging to Gerencia Materiales CAC-CNEA, Drs. F.S. Arico, M.J. Iribarren and P.B. Bozzano and technical staff by offering facilities for this research. PAF was supported by a Comisión Nacional de Energía Atómica (CNEA) professional fellowship.

APPENDIX A. Derivation of the equations for diffusion screening coarsening

The theory of diffusion-controlled particle coarsening developed by Lifshitz and Slyozov and Wagner (LSW) [19] is modified to take into account the volume fraction, ϕ, of precipitates. The modification is based on the supposition that the diffusion of solute to a growing particle (or from a shrinking particle) will depend on a distance characteristic of the spatial distribution of the particles in the polydisperse assembly. Steady-state diffusion under conditions of spherical symmetry is assumed. The characteristic distance is identified assuming that the Laplace diffusion potential is "cut off" by an exponential term over a screening length, r_D. Consequently, the flux of solute to the particle and, therefore, its growth rate, $(\frac{\partial r}{\partial t})$, are modified with respect to those predicted by the theory LSW. Specifically, both hypotheses are defined by Eqs. (1) and (2) in the main text.

The growth rate of the LSW theory is given by [19]:

$$\left(\frac{\partial r}{\partial t}\right)_{LSW} = \frac{2}{r} A\left(\frac{1}{r_c} - \frac{1}{r}\right) \tag{A.1}$$

The quantity A includes the interface energy γ of the precipitate and an averaged diffusion coefficient as was discussed in the main text. The radius $r_c(t)$ is the so-called critical radius, since obviously for $r>r_c$ growth and for $r<r_c$ shrinkage of the precipitate occurs. Then, a scaled growth rate can be derived from Eq. (2), of the main text, and (A.1) in terms of its normalized radius $\rho = r/r_c$ obtaining the relationship

$$\frac{\partial \rho}{\partial \tau} = \frac{A}{K_c}\left[\frac{2(\rho-1)(1+\rho/\rho_D)}{\rho^2}\right] - \rho \tag{A.2}$$

where $\tau = (1/3) ln r_c^3$; $K_c = dr_c^3/3dt$ and $\rho_D = r_D/r_c$. Lifshitz and Slyozov [19] proved that steady-state solutions to Eq. (A.2) are possible if and only if K_c is constant, the value of which can be determined by applying the following stability conditions, based on mass conservation in ρ space:

$$\left(\frac{d\rho}{d\tau}\right)\Big|_{\rho=\rho_{max}} = 0 \qquad \text{and} \qquad \left[\frac{d}{d\rho}\left(\frac{d\rho}{d\tau}\right)\right]\Big|_{\rho=\rho_{max}} = 0$$

The application of these stability conditions lead to the following results:

$$K_c = \frac{2}{\rho_{max}^3} A\left[2 - \rho_{max}\left(1 - \frac{1}{\rho_D}\right)\right] \tag{A.3}$$

where

$$\rho_{max} = 1 - \rho_D + \sqrt{\rho_D^2 + \rho_D + 1} \tag{A.4}$$

Now from the definition of K_c, the steady-state kinetic coarsening equation for the critical radius may be expressed as

$$r_c^3(t) - r_c^3(0) = 3 \quad K_c t \tag{A.5}$$

Here $r_c(0)$ is the critical radius within steady-state at some arbitrary initial time, $t = 0$.

Following the LSW argument [19], the normalized PSD, $G(\rho)$, which satisfies the continuity equation in ρ space is obtained from the expression

$$G(\rho) = \frac{B}{d\rho/d\tau} exp\left(\int_0^{\rho} \frac{1}{d\rho/d\tau} d\rho\right) \tag{A.6}$$

where B is the normalization constant determined by the condition $\int_0^{\infty} G(\rho) d\rho = 1$. The evaluation of Eq. (A.6) with $d\rho/d\tau$ given by the expression (A.2) was done in references [21,25] leading to

$$G(\rho) = \overline{\zeta}\, \frac{\rho^2 \exp\left[B_4/(\rho_{max}-\rho)\right]}{(\rho_{max}-\rho)^{-B_3}(\rho-\overline{\rho}_5)^{-B_5}} \text{ for } \rho \le \rho_{max}$$
$$G(\rho) = 0 \text{ for } \rho \ge \rho_{max} \tag{A.7}$$

The integration constant $\overline{\zeta}$ is calculated in an analogous way to B. The roots B_4 and $\overline{\rho}_5$ as well as the exponents B_3 and B_5 are functions of ρ_D and can be taken from reference [21]. Finally we can obtain the kinetic coarsening equation in terms of the average radius by combining Eq. (A.5) with the definition of the normalized average radius, $\langle\rho\rangle = \langle r\rangle/r_c$,

$$\langle r(t)\rangle^3 - \langle r(0)\rangle^3 = K(\phi) \quad t \tag{A.9}$$

$K(\phi)=3 \quad K_c\langle\rho\rangle^3$.

References

[1] H.K.D.H. Bhadeshia, Design of ferritic creep-resistant steels, ISIJ Int. 41 (2001) 626–640.
[2] S.M. Hao, T. Takayama, K. Ishida, T. Nishizawa, Miscibility gap in Fe-Ni-Al and Fe-Ni-Al-Co systems, Metall. Trans. A 15 (1984) 1819–1828.
[3] L. Eleno, K. Frisk, A. Schneider, Assessment of the Fe-Ni-Al system, Intermetallics 14 (2006) 1276–1290.
[4] C. Stallybrass, A. Schneider, G. Sauthoff, The strengthening effect of (Ni,Fe)Al precipitates on the mechanical properties at high temperatures of ferritic Fe–Al–Ni–Cr alloys, Intermetallics 13 (2005) 1263–1268.
[5] C. Stallybrass, G. Sauthoff, Ferritic Fe–Al–Ni–Cr alloys with coherent precipitates for high-temperature applications, Mater. Sci. Eng. A 387- 389 (2004) 985–990.
[6] T. Edahiro, K. Kouzai, H.Y. Yasuda, Mechanical properties and hardening mechanism of Fe–Al–Ni single crystals containing NiAl precipitates, Acta Mater. 61 (2013) 1716–1725.
[7] H. Calderon, M.E. Fine, Coarsening kinetics of coherent NiAl-type precipitates in Fe-Ni-Al and Fe-Ni-Al-Mo alloys, Mater. Sci. Eng. 63 (1984) 197–208.
[8] Z. Sun, G. Song, J. Ilavsky, G. Ghosh, P.K. Liaw, Nano-sized precipitate stability and its controlling factors in a NiAl-strengthened ferritic alloy, Sci. Rep. 5 (2015) 16081. http://dx.doi.org/10.1038/srep16081.
[9] S.M. Zhu, S.C. Tjong, J.K.L. Lai, Creep behavior of a β'(NiAl) precipitation strengthened ferritic Fe-Cr-Ni-Al alloy, Acta Mater. 46 (1998) 2969–2976.
[10] N.Q. Vo, C.H. Liebscher, M.J.S. Rawlings, M. Asta, D.C. Dunand, Creep properties and microstructure of a precipitation-strengthened ferritic Fe–Al–Ni–Cr alloy, Acta Mater. 71 (2014) 89–99.
[11] H.A. Calderon, M.E. Fine, J.R. Weertman, Coarsening and morphology of β´ particles in Fe-Ni-Al-Mo ferritic alloys, Metall. Trans. A 19 (1988) 1135–1146.
[12] Z.K. Teng, F. Zhang, M.K. Miller, C.T. Liu, S. Huang, Y.T. Chou, R.H. Tien, Y.A. Chang, P.K. Liaw, New NiAl-strengthened ferritic steels with balanced creep resistance and ductility designed by coupling thermodynamic calculations with focused experiments, Intermetallics 29 (2012) 110–115.
[13] P.Z. Zhao, T. Kozakai, T. Miyazaki, Phase separations into A2+DO_3 two phases in Fe-Al-V ternary ordering alloys, J. Jpn. Inst. Met. 53 (1989) 266–272.
[14] T. Maebashi, T. Kozakai, M. Doi, Phase equilibria in iron-rich Fe-Al-V ternary alloy system, Z. Met. 95 (2004) 1005–1010.
[15] P.R. Alonso, P.H. Gargano, P.B. Bozzano, G.E. Ramírez-Caballero, P.B. Balbuena, G.H. Rubiolo, Combined ab initio and experimental study of A2+$L2_1$ coherent equilibria in the Fe-Al-X (X=Ti, Nb, V) systems, Intermetallics 19 (2011) 1157–1167.
[16] P.A. Ferreirós, P.R. Alonso, P.H. Gargano, P.B. Bozzano, H.E. Troiani, A. Baruj, G.H. Rubiolo, Characterization of microstructures and age hardening of Fe_{1-2x} Al_x V_x alloys, Intermetallics 50 (2014) 65–78.
[17] C.K. Sudbrack, K.E. Yoon, R.D. Noebe, D.N. Seidman, Temporal evolution of the nanostructure and phase compositions in a model Ni-Al-Cr alloy, Acta Mater. 54 (2006) 3199–3210.
[18] L. Senčekova, M. Palm, J. Pešička, J. Veselý, Microstructures, mechanical properties and oxidation behaviour of single-phase $Fe_3Al(D0_3)$ and two-phase α-Fe,Al(A2)+ $Fe_3Al(D0_3)$ Fe-Al-V alloys, Intermetallics 73 (2016) 58–66.
[19] I.M. Lifshitz, V.V. Slyozov, The kinetics of precipitation from supersaturated solid solutions, J. Phys. Chem. Solids 19 (1–2) (1961) 35–50.
[20] A.J. Ardell, V. Ozolins, Trans-interface diffusion-controlled coarsening, Nat. Mater. 4 (2005) 309–316.
[21] J. Svoboda, F.D. Fischer, Generalization of the Lifshitz–Slyozov–Wagner coarsening theory to non-dilute multi-component systems, Acta Mater. 79 (2014) 304–314.
[22] A.J. Ardell, Trans-interface-diffusion-controlled coarsening in ternary alloys, Acta Mater. 61 (2013) 7749–7754.
[23] A.J. Ardell, The effect of volume fraction on particle coarsening: theoretical considerations, Acta Metall. 20 (1972) 61–71.
[24] B.A. Pletcher, K.G. Wang, M.E. Glicksman, Experimental, computational and theoretical studies of δ´ phase coarsening in Al–Li alloys, Acta Mater. 60 (2012) 5803–5817.
[25] A.D. Brailsford, P. Wynblatt, The dependence of Ostwald ripening kinetics on particle volume fraction, Acta Metall. 27 (1979) 489–497.
[26] K. Tsumuraya, Y. Miyata, Coarsening models incorporating both diffusion geometry and volume fraction of particles, Acta Metall. 31 (1983) 437–452.
[27] P.W. Voorhees, The theory of Ostwald Ripening, J. Stat. Phys. 38 (1985) 231–252.
[28] M.E. Glicksman, K.G. Wang, S.P. Marsh, Diffusional interactions among crystallites, J. Cryst. Growth 230 (2001) 318–327.
[29] P. Streitenberger, Analytical description of phase coarsening at high volume fractions, Acta Mater. 61 (2013) 5026–5035.
[30] C.J. Kuehmann, P.W. Voorhees, Ostwald Ripening in ternary alloys, Metall. Mater. Trans. A 27 (1996) 937–943.
[31] Y. Nishino, M. Kato, S. Asano, K. Soda, M. Hayasaki, U. Mizutani, Semiconductor like behavior of electrical resistivity in Heusler-type Fe_2VAl compound, Phys. Rev. Lett. 79 (1997) 1909–1912.
[32] Y. Iijima, K. Kimura, C. Lee, K. Hirano, Impurity diffusion and isotope effect of cobalt in α-iron, Mater. Trans. JIM 34 (1993) 20–26.
[33] C. Lee, Y. Iijima, T. Hiratani, K. Hirano, Diffusion of chromium in α-iron, Mater. Trans. JIM 31 (1990) 255–261.
[34] D.N. Torres, R.A. Perez, F. Dyment, Diffusion of tin in α-iron, Acta Mater. 48 (2000) 2925–2931.
[35] R.A. Perez, D.N. Torres, F. Dyment, Sb diffusion in α-Fe, Appl. Phys. A 81 (2005) 787–791.
[36] Y. Iijima, K. Kimura, K. Hirano, Self-diffusion and isotope effect in α-iron, Acta Metall. 31 (1988) 2811–2820.
[37] J. Crangle, G.M. Goodman, The magnetization of pure iron and nickel, Proc. R. Soc. Lond. A 321 (1971) 477–491.
[38] U.R. Kattner, B.P. Burton, Al-Fe (aluminum-iron), in: H. Okamoto (Ed.)Phase Diagrams of Binary Iron Alloys, ASM International, Materials Park, Ohio 44073-0002, USA, 1993, pp. 12–28.
[39] J.F. Smith, Fe-V (Iron-Vanadium), in: H. Okamoto (Ed.)Phase Diagrams of Binary Iron Alloys, ASM International, Materials Park, Ohio 44073-0002, USA, 1993, pp. 433–443.
[40] G. Neumann, C. Tuijn, Self-diffusion and impurity diffusion in pure metals, Pergamon materials series 14, Elsevier, UK, 2009, pp. 263–273.
[41] Y.H. Sohn, M.A. Dayananda, Interdiffusion, intrinsic diffusion and vacancy wind effect in Fe-Al alloys at 1000 °C, Scr. Mater. 40 (1999) 79–84.
[42] S. Peteline, E.M. Tanguep Njiokep, S. Divinski, H. Mehrer, Diffusion of solute elements in Fe_3Al, Defect Diffus. Forum 216–217 (2003) 175–180.
[43] H. Mehrer, M. Luckabauer, W. Sprengel, Self- and solute diffusion, interdiffusion and thermal vacancies in the system iron-aluminium, Defect Diffus. Forum 333 (2013) 1–25.
[44] M. Drechsler, J.F. Nicholas, On the equilibrium shape of cubic crystals, J. Phys. Chem. Solids 28 (1967) 2609–2627.
[45] C. Woodward, A. van de Walle, M. Asta, D.R. Trinkle, First-principles study of interfacial boundaries in Ni–Ni_3Al, Acta Mater. 75 (2014) 60–70.
[46] J.H. Westbrook, Temperature dependence of hardness of the equi-atomic iron group aluminides, J. Electrochem. Soc. 103 (1956) 54–63.
[47] P. Nagpal, I. Baker, Effect of cooling rate on Hardness of FeAI and NiAI,, Metall. Trans. A 21 (1990) 2281–2282.
[48] Y.A. Chang, L.M. Pike, C.T. Liu, A.R. Bilbrey, D.S. Stone, Correlation of the hardness and vacancy concentration in FeAl, Intermetallics 1 (1993) 107–115.
[49] L.M. Pike, C.T. Liu, Y.A. Chang, Effect of Ni on vacancy concentrations and hardness in FeAl alloys, Met. Mater. Trans. A 29 (1998) 1911–1915.
[50] W. Hüther, B. Reppich, Order hardening of MgO by large precipitated volume fractions of spinel particles, Mater. Sci. Eng. 39 (1979) 247–259.
[51] B. Reppich, Some new hardening aspects concerning particle mechanisms in γ´ precipitating Ni-base alloys-I: theoretical concept, Acta Metall. 30 (1982) 87–94.
[52] B. Reppich, Particle strengthening, in: H. Mughrabi (Ed.)Plastic Deformation and Fracture of Materials, Wiley-VCH, Weinheim, Germany, 1993, pp. 311–357.
[53] R. Taillard, A. Pineau, Room temperature tensile properties of Fe-19wt%Cr alloys precipitation hardened by the intermetallic compound NiAl, Mater. Sci. Eng. 56 (1982) 219–231.
[54] J.M. Rosenberg, H.R. Piehler, Calculation of the Taylor factor and lattice rotations for bcc metals deforming by pencil glide, Metall. Trans. 2 (1971) 257–259.
[55] D. Tabor, Indentation hardness: fifty years on a personal view, Philos. Mag. A 74 (1996) 1207–1212.
[56] R.B. Schwarz, R. Labusch, Dynamic simulation of solution hardening, J. Appl. Phys. 49 (1978) 5174–5187.
[57] W. Hüther, B. Reppich, Reppich, Interaction of dislocations with coherent, stress-free ordered particles, Z. Metallkde. 69 (1978) 628–634.
[58] U.F. Kocks, The theory of an obstacle-controlled yield strength, Mater. Sci. Eng. 27 (1977) 291–298.
[59] M.F. Ashby, Results and consequences of a recalculation of the Frank-Read and the Orowan stress, Acta Metall. 14 (1966) 679–681.
[60] R.A. Buckley, S. Kaviani, Some aspects of rapid solidification processing of Fe-Al-X alloys, Mater. Sci. Eng. A 258 (1998) 173–180.
[61] W. Köster, T. Gödecke, Physical measurements on iron-aluminum alloys between 10 and 50 at% Al. IV: the modulus of elasticity of the alloys, Z. Metallkde. 73 (1982) 111–114.
[62] B. Reppich, P. Schepp, G. Wehner, Some new hardening aspects concerning particle mechanisms in γ´ precipitating Ni-base alloys-II: experiments, Acta Metall. 30 (1982) 95–104.
[63] L.T.F. Eleno, L.A. Errico, P.G. Gonzales-Ormeño, H.M. Petrilli, C.G. Schön, Ordering phase relationships in ternary iron aluminides, Calphad 44 (2014) 70–80.
[64] G. deWit, J.S. Koehler, Interaction of dislocations with an applied stress in anisotropic crystals, Phys. Rev. 116 (1959) 1113–1120.
[65] A.J. Ardell, Precipitation hardening, Metall. Trans. A 16 (1985) 2131–2165.
[66] U.F. Kocks, A.S. Argon, M.F. Ashby, Thermodynamics and kinetics of slip, Prog. Mater. Sci. 19 (1975) 1–291.
[67] L.M. Brown, R.K. Ham, Dislocation particle interactions, in: A. Kelly, R.B. Nicholson (Eds.), Strengthening Methods in Crystals, Halsted Press Division, John Wiley & Sons, NY, 1971, p. 9.